Eur. Phys. J. D **27**, 131–146 (2003)
DOI: 10.1140/epjd/e2003-00251-1

THE EUROPEAN PHYSICAL JOURNAL D

Kinetic simulations of fuel ion transport in ICF target implosions

O. Larroche[a]

CEA DIF, B.P. 12, 91680 Bruyères-le-Châtel, France

Received 16 September 2002 / Received in final form 25 April 2003
Published online 12 August 2003 –

Abstract. A numerical code solving the ion Vlasov-Fokker-Planck kinetic equation is used to compute the hydrodynamics of the thermonuclear fuel in inertial confinement fusion pellets. Compared with standard hydrodynamics calculations, the kinetic results show enhanced ion transport between the core and the outer part of the target. Consequences are discussed in the case of plastic shells filled with deuterium gas and cryogenic deuterium-tritium targets envisioned for achieving ignition with megajoule-class lasers.

PACS. 52.25.Fi Transport properties – 52.65.Ff Fokker-Planck and Vlasov equation

1 Introduction — Motivation and aim of this study

In the numerical simulation [1] of the hydrodynamics of laser targets of interest for Inertial Confinement Fusion (ICF), ion transport is generally assumed negligible with respect to electron transport. Ion viscosity is usually not taken into account, in favor of numerical ("pseudo") viscosity. Ion thermal conduction is modeled in an approximate way, at best through Spitzer-Braginskii formulae [2,3], and non-Maxwellian features in the ion velocity distributions are always neglected.

However, some authors have investigated how kinetic effects might affect ion transport, possibly modifying the hydrodynamics and thermonuclear yield of those systems. References [4,5] considered from a theoretical point of view the direct effect of the loss of fast particles in the ion distribution on the nuclear reaction rate in ICF targets. They concluded that that mechanism might partially account for the neutron yield discrepancy found between experiments and one-dimensional (1D) hydrodynamics simulations, the main part of it being related to implosion symmetry defects which are not taken into account in 1D calculations.

On the other hand, direct kinetic calculations have been performed in simplified cases [6,7]. As a rule in those works, ion transport was found to be much more intense than usually assumed, with direct consequences on the nuclear reaction rate as suspected in references [4,5], but also, more importantly, indirect consequences through a modification of the target hydrodynamics.

This was also suspected in standard hydrodynamics simulations of the implosion of microballoons filled with DT gas where real viscosity was used instead of pseudoviscosity [8]. In that work, a lower fuel compression and a higher ion temperature were found, and there were no more well-defined shock fronts. However in that specific case, in contradiction with the estimates of references [4,5], the overall effect on neutron yield was an increase instead of the decrease needed to account for experimental results.

This paper presents kinetic numerical simulations, performed with our ion Fokker-Planck code FPion, of the hydrodynamics and neutron yield in targets which are more relevant to ICF due to their larger size and fuel content, but which are thus much more collisional, which makes those simulations more difficult. Those targets include, on one hand, microballoons filled with D_2 gas [9], and on the other hand, targets envisioned for achieving ignition with next-generation, megajoule-size, lasers such as the National Ignition Facility (NIF) in the USA [10] and the Laser Mégajoule (LMJ) in France [11].

In the first case, we wish to examine whether anomalous ion transport might account for the neutron yield discrepancy between experiments and the 1D numerical simulation with the code LILAC presented in reference [9]. The explanation usually put forward is the hot-spot/cold-fuel or fuel/pusher mixing due to Rayleigh-Taylor instabilities during the shell slowing-down stage leading to target stagnation (see the review papers [12–15] and references therein). However, it has been argued [16] that that explanation should only apply to neutrons produced during the compression stage, but not to the first neutron burst released during the main shock collapse in the centre of the target (around $t = 1.7$ ns in Figs. 1 and 2), which leaves the problem open as far as that part of the neutron yield curve is concerned.

In the second case, we wish to re-examine the points raised in the past [4,5] as to the behaviour of ICF targets, in view of upcoming experiments aimed at demonstrating ignition on facilities such as the NIF and the LMJ,

[a] e-mail: olivier.larroche@cea.fr

using present-day computational resources which are vastly larger than those available to the authors of references [4,5] who could only resort to analytical order-of-magnitude estimates.

Those very computing-time-expensive kinetic simulations become realizable today thanks to the improvement of computers, and to various technical steps to be described below. In particular, the kinetic computation is only applied to the inner part of the target where nuclear reactions take place (the "fuel") but neither to the surrounding confinement shell (the "pusher") nor to the fuel/pusher interface where specific kinetic effects might occur. Also discussed here is the applicability to systems of macroscopic size, possibly including highly collisional regions, of methods whose natural scale length is the particle collision mean free path.

In Section 2, the underlying physical model is presented, along with the improvements to the code FPion implementing that model which were necessary to make those simulations possible, and caution needed when interpreting the results. In Section 3, a kinetic simulation of the D_2 targets of reference [9] is presented, in view of the long-standing problem of the neutron yield deficit. In Section 4, a simulation of hot-spot formation in an ICF target is presented, aiming at assessing kinetic effects on the ignition process. Section 5 gives a conclusion and describes ongoing work on the kinetic treatment of thermonuclear combustion.

2 Ion Fokker-Planck modeling of ICF target hydrodynamics

2.1 The physical model

The physical basis of the code FPion is the Vlasov-Fokker-Planck equation governing the velocity distribution function in spherical one-dimensional geometry $f_i(r, v_r, v_\perp)$ for one or more ion species indexed by subscript i, with atomic mass A_i and charge Z_i, where r is the spatial radius, v_r and $v_\perp$ are the radial and tangential components of the velocity respectively, and azimuthal symmetry around v_r in velocity space holds due to the assumed spherical symmetry in configuration space. This equation is expressed in the units defined in Table 1:

$$\frac{\partial f_i}{\partial t} + v_r \frac{\partial f_i}{\partial r} + \frac{v_\perp}{r}\left(v_\perp \frac{\partial f_i}{\partial v_r} - v_r \frac{\partial f_i}{\partial v_\perp}\right) + \frac{\mathcal{E}_i}{A_i}\frac{\partial f_i}{\partial v_r} = \sum_{j=1}^{n}\left(\frac{\partial f_i}{\partial t}\right)_{ij} + \frac{1}{2\tau_{ei}}\frac{\partial}{\partial v_\alpha}\left[(v_\alpha - u_{i\alpha}) f_i(\mathbf{v}) + \frac{T_e}{A_i}\frac{\partial f_i}{\partial v_\alpha}(\mathbf{v})\right] \quad (1)$$

where $\mathcal{E}_i$ is the effective electric field applied to ions of species i, defined by the following expression:

$$\mathcal{E}_i = -\frac{Z_i}{n_e}\frac{\partial P_e}{\partial r} \quad (2)$$

Table 1. Units defined from reference values of the particle density n_0 and particle thermal energy $k_B T_0$. In the text the word *temperature* will be used in lieu of *reduced thermal energy*.

Quantity	Unit
density	n_0 (arbitrary reference value)
thermal energy	$k_B T_0$ (arbitrary reference value)
time	$\tau_0 = \frac{(k_B T_0)^{3/2} m_p^{1/2}}{4\pi e^4 n_0}$
length	$\lambda_0 = (k_B T_0/m_p)^{1/2}\tau_0 = \frac{(k_B T_0)^2}{4\pi e^4 n_0}$
velocity	$v_0 = (k_B T_0/m_p)^{1/2} = \lambda_0/\tau_0$
distribution function	$f_0 = n_0/v_0^3$
first Rosenbluth pot.	$\mathcal{S}_0 = n_0/v_0$
second Rosenbluth pot.	$\mathcal{T}_0 = n_0 v_0$
electric field ($\mathcal{E}_i$)	$E_0 = m_p v_0^2/\lambda_0 = m_p \lambda_0/\tau_0^2$
heat flux	$Q_0 = \frac{n_0 (k_B T_0)^{3/2}}{m_p^{1/2}}$

where

$$n_e = \sum_{j=1}^{n} Z_j n_j,$$

T_e and P_e are the electron density, temperature and pressure respectively, and $n_i = \int f_i(\mathbf{v})\mathrm{d}^3 v$ is the density of ions of species i, $u_{i\alpha} = (1/n_i)\int v_\alpha f_i(\mathbf{v})\mathrm{d}^3 v$ is the α component of their mean velocity (component u_r alone being non-zero from symmetry). In the above expression for $\mathcal{E}_i$ we discarded electron-ion friction terms which introduce additional differential forces when more than one ion species are present, and also the thermal force arising from the electron heat flux (see, *e.g.*, [3]). The form (2) for the electric field arises from the quasineutrality approximation together with the smallness of the electron mass. Terms on the r.h.s. of equation (1) are Fokker-Planck terms modeling Coulomb collisions in the ideal plasma limit, dominated by small deviations [17]. The Coulomb logarithms $\mathrm{Log}\Lambda_{ab}$ are defined in reference [3]. The electron-ion collision term involves the following value of the relevant collision time:

$$\tau_{ei} = \frac{3\sqrt{\pi} A_i T_e^{3/2}}{2\epsilon\sqrt{2} Z_i^2 n_e \mathrm{Log}\Lambda_{ie}}$$

where $\epsilon = (m_e/m_p)^{1/2} \approx 0.0233$ (m_e and m_p are the electron and proton masses respectively). The ion-ion collision term is [17]:

$$\left(\frac{\partial f_i}{\partial t}\right)_{ij} = \frac{4\pi Z_i^2 Z_j^2}{A_i^2}\mathrm{Log}\Lambda_{ij} \times \frac{\partial}{\partial v_\alpha}\left[\frac{A_i}{A_j}\frac{\partial \mathcal{S}_j}{\partial v_\alpha} f_i - \frac{\partial^2 \mathcal{T}_j}{\partial v_\alpha \partial v_\beta}\frac{\partial f_i}{\partial v_\beta}\right]$$

where $\mathcal{S}_j$ and $\mathcal{T}_j$ are the so-called Rosenbluth potentials:

$$\mathcal{S}_j = -\frac{1}{4\pi}\int \frac{f_j(\mathbf{v}')}{|\mathbf{v} - \mathbf{v}'|}\mathrm{d}^3 v'$$

and

$$\mathcal{T}_j = -\frac{1}{8\pi}\int |\mathbf{v} - \mathbf{v}'|\, f_j(\mathbf{v}')\mathrm{d}^3 v'.$$

The above integrals will be computed by solving the Poisson equations in velocity space: $\Delta_v \mathcal{S}_j = f_j$ and $\Delta_v \mathcal{T}_j = \mathcal{S}_j$ with appropriate boundary conditions. We thus do not assume the Rosenbluth potentials to be isotropic as is usually done in fast-particle slowing-down models (see, *e.g.*, [18]). Also energy diffusion is treated instead of using the assumptions usually made in neutron-transport-like models [19]. The latter hypotheses are necessary in our case because large distortions in the distribution are expected, but no highly suprathermal velocities (see Ref. [6]).

As far as electrons are concerned, only an equation for the temperature (or, equivalently, the energy density) is needed since in one-dimensional geometry the density and velocity are known from the quasineutrality assumption. The electron energy density W_e is governed by the following equation:

$$\frac{\partial W_e}{\partial t} + \frac{1}{r^2}\frac{\partial}{\partial r}\left(r^2 u_e W_e\right) + \frac{1}{r^2}\frac{\partial}{\partial r}\left(r^2 u_e\right) P_e - \frac{1}{r^2}\frac{\partial}{\partial r}\left(r^2 \kappa_e \frac{\partial T_e}{\partial r}\right) = \sum_{j=1}^{n} \frac{3 n_j}{2\tau_{ej}}\left(T_j - T_e\right) + \left(\frac{\partial W_e}{\partial t}\right)_{\mathrm{rad}} \tag{3}$$

where κ_e is Spitzer's thermal conductivity in the presence of several ion species (see Appendix of Ref. [20]), the collision time τ_{ej} has been defined above and T_j is the temperature of ions of species j in reduced units:

$$T_{j\parallel} = \frac{1}{n_j}\int A_j \left(v_r - u_{j\parallel}\right)^2 f_j(\mathbf{v}) \mathrm{d}^3 v$$
$$T_{j\perp} = \frac{1}{2 n_j}\int A_j v_\perp^2 f_j(\mathbf{v}) \mathrm{d}^3 v$$
$$T_j = \frac{T_{j\parallel} + 2 T_{j\perp}}{3}.$$

The electron energy density W_e and pressure P_e are given by the equation of state of the electron fluid, which in the limit of a tenuous plasma reduces to the well-known form:

$$W_e(n_e, T_e) \xrightarrow[n_e \to 0]{} \frac{3}{2} n_e T_e$$
$$P_e(n_e, T_e) \xrightarrow[n_e \to 0]{} n_e T_e.$$

In the present case the electron equation of state will take into account Fermi degeneracy using the well-known formulae (see, *e.g.*, [21]) expressed below in dimensional, non-reduced units:

$$n_e = 4\pi \left(\frac{2 m_e k_B T_e}{h^2}\right)^{3/2} I_{1/2}(z)$$
$$W_e = \frac{3}{2} P_e = 4\pi \left(\frac{2 m_e k_B T_e}{h^2}\right)^{3/2} k_B T_e I_{3/2}(z)$$

where h is Planck's constant and $I_{n/2}$ is the so-called "Fermi integral":

$$I_{n/2}(z) = \int_0^\infty \frac{y^{n/2}}{z^{-1}\mathrm{e}^y + 1} \mathrm{d}y.$$

In equation (3) electron-ion friction and thermal force terms were neglected, as in equation (1).

For discretization all terms involving Rosenbluth potentials are summed up for each ion species i, including potentials $\mathcal{S}_{ie}$ and $\mathcal{T}_{ie}$ modeling the electron collision term in the limit of electron velocities large with respect to the ion velocities; the full collision term for species i thus finally reads:

$$\left(\frac{\partial f_i}{\partial t}\right)_{i,\mathrm{coll}} = \frac{\partial}{\partial v_\alpha}\left[\frac{\partial \mathcal{S}_i'}{\partial v_\alpha} f_i - \frac{\partial^2 \mathcal{T}_i'}{\partial v_\alpha \partial v_\beta}\frac{\partial f_i}{\partial v_\beta}\right]$$

with

$$\mathcal{S}_i' = \sum_{j=1}^{n} \frac{4\pi Z_i^2 Z_j^2 \mathrm{Log}\Lambda_{ij}}{A_i A_j}\mathcal{S}_j + \mathcal{S}_{ie}$$
$$\mathcal{T}_i' = \sum_{j=1}^{n} \frac{4\pi Z_i^2 Z_j^2 \mathrm{Log}\Lambda_{ij}}{A_i^2}\mathcal{T}_j + \mathcal{T}_{ie}$$

and the electron Rosenbluth potentials read:

$$\mathcal{S}_{ie} = \frac{(v_x - u_i)^2 + v_\perp^2}{4\tau_{ei}}$$
$$\mathcal{T}_{ie} = -\frac{T_e}{A_i}\frac{(v_x - u_i)^2 + v_\perp^2}{4\tau_{ei}}.$$

Overall energy conservation in collisions is ensured by assigning to electrons the energy lost by ions in the process described by the above equation.

The radiation coupling term (with subscript "rad") on the r.h.s. of equation (3) only includes Bremsstrahlung losses [22]:

$$\left(\frac{\partial W_e}{\partial t}\right)_{\mathrm{rad}} = -P_{\mathrm{rad}}$$

where

$$P_{\mathrm{rad}} = 4.14 \times 10^{-4} T_0(\mathrm{keV}) n_e T_e^{1/2} \sum_i n_i Z_i^2$$

and T_0 is the reference temperature defined in Table 1.

2.2 Improvements to the code

The implementation of the code FPion which numerically solves equations (1) and (3) has been briefly accounted for in other papers [6,23]. Here we will describe the modifications which proved necessary for applying the code to the implosion of spherical targets of macroscopic size. The reader who does not feel concerned about the technicalities of numerical modeling may want to skip the rest of this section and go directly to Sections 3 and 4 where simulation results are discussed.

These improvements were needed because working with realistic systems where densities, temperatures, and hence particle collision times span several decades is not feasible within a reasonable computing time unless special steps are taken, and this in turn needs some refined understanding of the physical processes involved. The following subsections deal with the interplay between those physical processes and numerical methods that implement them in realistic situations.

2.2.1 Zoning scheme

The original version of the code FPion used a rectangular numerical grid with equal mesh sizes in the three directions r, v_r and $v_\perp$. This is well adapted to the simulation of systems where density and temperature contrasts are not too large, such as the shock-wave problem of reference [6]. In addition, using such a zoning scheme, when possible, greatly simplifies the computation of advection in plane geometry, and even in spherical geometry since it allows a global description of the distribution using cubic splines, as was done in reference [7].

In less academic cases, particularly for the implosion of ICF targets, density and temperature can span several decades, forbidding the use of a regular grid if computing time and RAM and disk space are to be kept within realistic values. It is thus necessary to use a spatial grid with a varying mesh size and a velocity grid whose mesh size and radial offset are adjusted to the local parameters of the distribution, to take into account variations of the temperature and average velocity over space and time. The velocity grid at each point in space is otherwise regular. More specifically we use:

$$v_{rj} = j\delta v + v_0 \qquad \text{for} \quad -j_{\max}/2 \le j \le j_{\max}/2$$
$$v_{\perp k} = (k - 1/2)\delta v \quad \text{for} \quad 0 \le k \le k_{\max}$$

where δv is the velocity mesh size and v_0 is a radial velocity reference. Cells with $k = 0$ having a negative perpendicular velocity are introduced to make the application of the boundary condition on the distribution on the velocity axis easier:

$$\left(\frac{\partial f_i}{\partial v_\perp}\right)(v_\perp = 0) = 0.$$

Cells with $k = k_{\max}$ or $j = \pm j_{\max}/2$ are assigned a vanishing distribution value, thus implementing the boundary condition for the collision term.

The grid defined as above by a set of local values of the central velocity v_0 and mesh size δv is advanced before each advection step by a relaxation process towards a state where the central velocity is equal to the hydrodynamic velocity u and the velocity increment is such that $v_{\rm th}/\delta v = v_{\max}/v_{\rm th}$ where $v_{\rm th}$ is the thermal velocity and $v_{\max} = \delta v \times j_{\max}/2$. The routine in charge of that relaxation process receives values of $v_{\rm th}$ and u taking into account particles from neighbouring cells which may enter the cell under consideration due to advection.

2.2.2 Advection

The methods used by various authors for solving the kinetic equation fall in two broad categories. The first one includes codes derived from neutron transport theory, using a multigroup or finite-element approach, which are well-adapted to the slowing-down of fast particles on a given thermal background, where the collision operator can be reduced to the sum of a slowing-down term with no energy diffusion and an energy-conserving angular scattering term. This approximation is allowed when the Rosenbluth potentials can be assumed to be isotropic (see, *e.g.*, [18,19,24,25]). Those methods are not adapted to our case where there is no such clear separation between fast particles and a thermal background, so that full nonlinear Fokker-Planck terms should be retained, and the Rosenbluth potentials should be consistent with the distribution for angular dependencies to be treated correctly.

The second code category uses splitting schemes working either directly through shift and interpolation in phase space of a finite-difference representation of the distribution (see, *e.g.*, [26–28]) or indirectly in a transformed space (for example Fourier transform [29]). In the latter category, Vidal [7] performs a shift and interpolation of a cubic-spline representation of the distribution function along the three directions r, v_r, $v_\perp$ which seems well-behaved in the whole phase space, but cannot be directly applied to the particular grid scheme that we use (it can be easily applied only to a global rectangular grid over all three directions). We thus developed a hybrid method which is presently described.

The transformation of the phase-space coordinates r, v_r, $v_\perp$ during one time step δt is computed in the following way:

$$r(t + \delta t) = \sqrt{r(t)^2 + 2r(t)v_r(t)\delta t + v^2\delta t^2} \tag{4}$$

$$v_r(t + \delta t) = \frac{r(t)v_r(t) + v^2\delta t}{r(t + \delta t)} \tag{5}$$

$$v_\perp(t + \delta t) = \frac{r(t)v_\perp(t)}{r(t + \delta t)}. \tag{6}$$

The above formulae are applied backwards in time (inserting a negative time increment) for every node of the grid, and the position with respect to the grid of the starting point thus defined is computed. The distribution is then interpolated over the three directions r, v_r, $v_\perp$. Since the velocity grid varies from one space mesh to the next, the cubic-spline interpolation method cannot be used globally as in reference [7]. We thus use it in velocity space only for each space mesh, with the same boundary conditions as in the work of Vidal *et al.* [7], namely "not-a-knot" (see Ref. [30] about splines) in v_r and on the upper $v_\perp$ boundary, and a vanishing derivative at $v_\perp = 0$ (that is midway between the first two grid points $k = 0$ and $k = 1$). The target point in phase space is chosen at cell centre, that is with the above notations at $v_r = v_{rj}$, $v_\perp = v_{\perp k}$ and $r = r_{ci} = (r_{i-1} + r_i)/2$ where r_i for $i = 0$ to $i_{\max}$ is the position of the upper boundary of the ith space mesh. We then perform a cubic interpolation between neighbouring space points i and $i+1$ keeping the values of the distribution f on nodes f_i and f_{i+1} fixed, as well as the derivative $\partial f/\partial r$ there, the latter being estimated by the centred difference $(f_{i+1} - f_{i-1})/(r_{ci+1} - r_{ci-1})$, limited in such a way that no new extremum of f can appear in cell i, that is between r_i and r_{i-1}.

The simulation is initialized from density, velocity and temperature profiles (which in the present case are taken

from a previous hydrodynamics simulation) from which a Maxwellian ion distribution is calculated in each spatial mesh. The boundary condition on the outer limit of the space domain is also a Maxwellian distribution deduced from temporal profiles of the same hydrodynamic quantities recorded at the given space-dependent position.

2.2.3 Acceleration

In this stage the part of the Vlasov equation (the l.h.s. of Eq. (1)) which accounts for the electric field:

$$\frac{\partial f_i}{\partial t} + \frac{\mathcal{E}_i}{A_i}\frac{\partial f_i}{\partial v_r} = 0 \tag{7}$$

is solved; the effective field $\mathcal{E}_i$ is defined by equation (2). Since in this process the ion energy changes, a conservative scheme is obtained by computing the work of electron pressure forces at the same time, as will be described in more detail in Section 2.2.5 which deals with the treatment of electrons. Indeed, taking moments over v_r and v_r^2 of equation (7), we respectively obtain (since the density n_i remains fixed is the acceleration process):

$$\frac{\partial}{\partial t}(A_i u_i) = \mathcal{E}_i$$

$$\frac{\partial}{\partial t}(E_{cri}) = n_i u_i \mathcal{E}_i$$

where

$$E_{cri} = \frac{A_i}{2}\int v_r^2 f_i \mathrm{d}^3 v = \frac{1}{2}A_i n_i u_i^2 + \frac{1}{2}n_i T_{ir}$$

is the kinetic energy density in the radial direction of particles of species i. Summing the latter equation over species, taking into account the expression (2) for the effective electric field and the quasineutrality condition, leads to:

$$\frac{\partial}{\partial t}\sum_i E_{cri} = -u_e \frac{\partial P_e}{\partial r}$$

which states that the kinetic energy gained by the ions during acceleration is indeed lost by electrons, being equal to the opposite of the r.h.s. of equation (9) (see Sect. 2.2.5).

2.2.4 Fokker-Planck collision term

The numerical methods for advancing the Fokker-Planck collision term are described in detail in reference [23], and since that part of the code was only slightly modified we will only give a broad outline of it here.

The Fokker-Planck operator is a diffusion term in velocity space (hence formally two-dimensional in the present case), which is treated by an alternate-direction implicit method [31]. Since the diffusion tensor itself linearly depends on the distribution through the Rosenbluth potentials, we perform an iterative resolution which leads to a formally time-centred scheme. The calculation of the Rosenbluth potentials requires to solve two Poisson equations in velocity space with non-vanishing boundary conditions. However, we recover a vanishing Dirichlet boundary condition by first computing an explicit approximate value for the potentials deduced from their multipolar expansion [32], the solution of the Poisson equations being performed only for the residual part of the potentials.

The recent developments which were necessary for implosion simulations are described in more detail below.

Time step adaptation and acceleration of electron collisions. For accuracy reasons, since the scheme is not purely implicit and is not well-behaved when the time step δt becomes greater than the collision time, the collision step is sub-cycled on a time step δt_0 close to the smallest collision time encountered in the distribution, which *a priori* leads to $N_c = \delta t/\delta t_0$ sub-iterations. At the end of every sub-iteration, the distribution variation is examined, and if it is found to be less than a prescribed rate the sub-cycling loop is interrupted, assuming that the distribution has come close to equilibrium. This is expected to occur in the simulation of realistic systems where the calculation is focussed on kinetic effects in moderately collisional regions, while in other parts of the computational domain very collisional regions are found, where one only wants to recover thermodynamic equilibrium wasting as little computing time as possible.

The application of the latter idea is complicated by the existence of several, possibly very different, collisional time scales. For definiteness, we will assume that there are essentially two collision frequencies, namely an ion collision frequency ω_i and an electron-ion collision frequency ω_e, *a priori* with $\omega_e \ll \omega_i$. To treat ion collisions the time step δt will be split into N_{ci} sub-iterations over a time $\delta t_0 = \delta t/N_{ci}$ (which is chosen to be of the order of $1/\omega_i$), and the sub-iteration loop will possibly be interrupted after $N < N_{ci}$ cycles. Then, if nothing else is done the electron collision efficiency will hence be cut down by a factor N/N_{ci}.

To correctly account for electron-ion collisions in spite of a reduced number of sub-iterations, the corresponding collision term (and thus the frequency ω_e) must be multiplied by an acceleration factor to advance the computation of electron collisions as much as possible in the first sub-iterations. We can then be in one of two cases:

- either $\omega_e < 1/\delta t$, and ω_e can be multiplied by a factor $\delta t/\delta t_0$, which completes the calculation of electron collisions in $N_{ce} = 1$ sub-iteration while keeping the per-iteration variation rate $\delta t_0 \times (\delta t/\delta t_0)\omega_e$ less than 1 for this term;
- or $1/\delta t_0 > \omega_e > 1/\delta t$ (δt_0 is computed in such a way that the first inequality is always satisfied), in which case the acceleration factor must not exceed $1/(\omega_e \delta t_0)$ to keep the per-iteration variation rate below 1, and then *a priori* $N_{ce} = \omega_e \delta t$ sub-iterations are needed to fully account for electron collisions. However we can then use the same criterion on the relative variation of

the distribution to stop sub-cycling as in the case of ion collisions.

To summarize, in practice we first compute the numbers of iterations needed by the electron and ion collision terms, respectively:

$$N_{ce} = 1 + E\left(\omega_e \delta t\right)$$

and

$$N_{ci} = 1 + E\left(\max(\omega_i, \omega_e)\delta t\right)$$

where $E(x)$ stands for the integer part of x, then the sub-cycle time step δt_0 and the acceleration factor α:

$$\delta t_0 = \delta t / N_{ci} \qquad \text{and} \qquad \alpha = \frac{N_{ci}}{N_{ce}}$$

and the electron collision frequency is made to vanish after N_{ce} sub-iterations.

BGK collisions and instantaneous thermalization. In various cases, it can be useful to have a simpler collision term available. We thus implemented, in addition of the full Fokker-Planck term, a multispecies Bhatnagar-Gross-Krook collision term [33] which also accounts for electron-ion collisions, following reference [34].

When ion collision times are very small, one can even go beyond that and merely replace the ion-ion collision term with an instantaneous thermalization of the distribution with velocity and temperature values corresponding to a complete relaxation to equilibrium.

2.2.5 Electron treatment

Equation (3) for the electron temperature, which we will re-state in the more compact form:

$$\frac{\partial W_e}{\partial t} + \mathbf{div}\left(u_e W_e\right) + P_e \mathbf{div} u_e + \mathbf{div} Q_e = \left(\frac{\partial W_e}{\partial t}\right)_{ei} + \left(\frac{\partial W_e}{\partial t}\right)_{\text{rad}} \quad (8)$$

accounts for several mechanisms affecting the electron temperature, namely, internal energy convection by the velocity field u_e, the work of electron pressure forces during that convection and thermal conduction through the heat flux Q_e. On the r.h.s. are terms accounting for the collisional energy exchange with ions and energy exchange with radiation. Each of those mechanisms will be treated in turn, together with its counterpart from the point of view of the ions, which more readily leads to a globally energy-conserving scheme. It should be noticed right now that the collisional heating term is automatically taken into account in the kinetic treatment of the collisions undergone by the ions, as described in Section 2.1.

Electron convection. The convective part of the electron treatment, corresponding to the first part of equation (8) for the energy density:

$$\left(\frac{\partial W_e}{\partial t}\right)_{\text{conv}} + \mathbf{div}\left(u_e W_e\right) = 0$$

is treated in the ion advection routine, using the velocity field u_e deduced from the ion velocities computed in that routine for the convection of the initial density $W_e(n_e, T_e)$, the updated value of the temperature being obtained after convection through the equation of state from the updated energy density and the updated number density n_e deduced from the ion densities just computed. This is also where the electron temperature value on the right edge of the space domain is imposed in the case of a boundary condition deduced from an externally fixed thermal equilibrium.

Work of the pressure and electric forces. The work of the pressure and electric forces is modeled by the second part of equation (8):

$$\left(\frac{\partial W_e}{\partial t}\right)_{pdv} + P_e \mathbf{div} u_e = 0$$

which can be set into the form of an inhomogeneous conservation equation:

$$\left(\frac{\partial W_e}{\partial t}\right)_{pdv} + \mathbf{div}(u_e P_e) = u_e \frac{\partial P_e}{\partial r}. \quad (9)$$

In that alternate form, the second term on the l.h.s. accounts for the power per unit volume of electron pressure forces exerted on the ends of a volume element of thickness $r' - r = \delta r$ and cross-section $S(r)$:

$$-\mathbf{div}(u_e P_e) = \lim_{r' \to r} \frac{S(r)P_e(r)u_e(r) - S(r')P_e(r')u_e(r')}{S(r)\delta r}.$$

The term on the r.h.s. is the power transferred to electrons per unit volume by the electric field which, neglecting friction corrections, reads (see Eq. (2)):

$$\mathcal{E} = -\frac{1}{n_e}\frac{\partial P_e}{\partial r}.$$

To ensure overall energy conservation, it is thus advisable to treat that part of the electron equation in its second form (9) together with ion acceleration by the electric field, assigning the kinetic energy lost by the ions in that process to the electron thermal energy (which completes the treatment of the electric term on the r.h.s. of Eq. (9)), using the divergence form of the pressure force term (second term on the l.h.s. of Eq. (9)).

Electron thermal conduction. The third part of the electron equation (8):

$$\left(\frac{\partial W_e}{\partial t}\right)_{\text{cond}} + \mathbf{div} Q_e = \left(\frac{\partial W_e}{\partial t}\right)_{\text{rad}}$$

takes into account thermal conduction and radiative losses. It will be treated using a standard heat equation solving module, with Spitzer's thermal conductivity [2] and a Dirichlet boundary condition based on the pre-existing temperature values in the boundary cells. In spherical geometry, since the cell section $S(r)$ vanishes at the centre, this automatically yields the required vanishing heat flux condition there.

2.2.6 Diagnostics

The distribution function computed by FPion is periodically recorded on disk files from which various quantities can then be calculated in a post-processing stage, such as the parallel distribution function (integrated over $v_\perp$) as a function of r and v_r, spatial profiles of moments of order 0 to 3 of the distribution, particularly temperatures and pressures along the longitudinal and transverse directions leading to the distribution anisotropy, the heat fluxes corresponding to the longitudinal and transverse degrees of freedom and the ratios of those fluxes to the corresponding free-streaming flux. The following definition is used of the free-streaming heat flux for a particle species with mass m, temperature T, and density n:

$$Q_{\rm FS} = n v_{\rm th} k_B T = \frac{n (k_B T)^{3/2}}{m^{1/2}}.$$

Hence the electron and ion free-streaming fluxes respectively read, in reduced units:

$$Q_{e\rm FS} = n_e \frac{T_e^{3/2}}{\epsilon}$$

$$Q_{i\rm FS} = n_i \frac{T_i^{3/2}}{A^{1/2}}$$

in terms of the heat flux unit Q_0 defined in Table 1.

The post-processing also includes the calculation of the rate of the nuclear reactions of interest in the cases under study, namely, the reaction $\mathrm{D} + \mathrm{D} \rightarrow n + {}^3\mathrm{He}$ in the case of the D_2-filled capsules of reference [9], and the reaction $\mathrm{D} + \mathrm{T} \rightarrow n + {}^4\mathrm{He}$ for the LMJ/NIF targets. Those rates are computed either using the Maxwellian reactivity deduced from the ion temperature and density values recorded in the simulation, or by direct integration against the full ion distribution function, using in both cases the cross-section parametrizations of reference [35]. This allows a discrimination to be made between the direct effect on reactivity of modifications in the shape of the ion distribution function and indirect effects due to changes in the ion density and temperature.

2.3 Proper usage of the code and interpretation of the results

2.3.1 About boundary conditions

The general principle of the simulations to be described below is to start from an initial condition based on a previous hydrodynamics calculation, and perform a kinetic computation of the behaviour of the fuel with a boundary condition corresponding to the hydrodynamic quantities recorded as a function of time on the fuel/pusher interface in the hydrodynamics calculation. The kinetic boundary condition imposes the ingoing part of the local Maxwellian on the boundary while outgoing particles are free. This procedure accounts neither for a possible interdiffusion of the fuel and pusher particles nor for the heat transport across the fuel/pusher interface which might be important, as discussed in reference [7]. However, it will be checked that in the case of the more collisional targets treated in this work, as opposed to the simulations of reference [7], for most of the implosion duration the computed distribution on the boundary remains close to the local Maxwellian, which eliminates the uncertainties related to the modeling of heat transport on the boundary which were a problem in interpreting the results of that work.

2.3.2 About the time step

Although there is formally no CFL-like constraint on the time step, one might still ask whether particles can be safely advected over distances larger than their collision mean free path during one advection step, because due to the splitting scheme retained, collisions are effectively turned off during the advection step. The region of velocity space where that constraint is the most restrictive is the thermal particle region, taking into account the velocity dependency of the Coulomb collision mean free path. For those particles, the validity condition is expected to be of the form $\delta t < \tau_i$ where τ_i is a typical collision time. This is far too restrictive in strongly collisional regions where the distribution is close to equilibrium but the time step is much larger than the collision time; in those regions it would be desirable to use a reasonably large value of the time step, without taking the above constraint into account. We will presently show that this is indeed possible.

Leaving aside the acceleration term proportional to the electric field for the sake of the present discussion, the Fokker-Planck equation to be solved reads:

$$\frac{\partial f}{\partial t} + v_x \frac{\partial f}{\partial x} = \left(\frac{\partial f}{\partial t}\right)_{\rm coll}. \tag{10}$$

The first three moments of this equation are obtained by multiplying by 1, v_x and v^2 and integrating over v, and lead to the usual hydrodynamics equations:

$$\frac{\partial n}{\partial t} + \frac{\partial}{\partial x}(nu) = 0$$

$$\frac{\partial u}{\partial t} + u\frac{\partial u}{\partial x} + \frac{1}{mn}\frac{\partial P_x}{\partial x} = 0$$

$$\frac{3}{2}\left(\frac{\partial P}{\partial t} + u\frac{\partial P}{\partial x}\right) + \frac{5P}{2}\frac{\partial u}{\partial x} + \delta P \frac{\partial u}{\partial x} + \frac{\partial Q}{\partial x} = 0$$

where m is the particle mass, n, u and P_x are the fluid density, velocity and longitudinal pressure respectively,

$P = (P_x + 2P_\perp)/3$ is the isotropic part of the pressure, $\delta P = P_x - P$ is the pressure anisotropy and Q is the heat flux. The r.h.s. of those equations vanishes due to the properties of the collision term, which conserves mass, momentum and energy exactly. An equation for the pressure anisotropy is found by integrating equation (10) over v_x^2 and $v_\perp^2$ separately and subtracting:

$$\frac{3}{2}\left(\frac{\partial \delta P}{\partial t} + u\frac{\partial \delta P}{\partial x}\right) + 2P\frac{\partial u}{\partial x} + \frac{7}{2}\delta P\frac{\partial u}{\partial x} + \frac{\partial \delta Q}{\partial x} = \frac{3}{2}\left(\frac{\partial \delta P}{\partial t}\right)_{\text{coll}} \quad (11)$$

where

$$\delta Q = m\int (v_x - u)\left((v_x - u)^2 - \frac{1}{2}v_\perp^2\right) f \mathrm{d}^3 v.$$

In the case of strongly collisional systems evolving on a slow (hydrodynamic) time scale, equation (11) tells us that the (small) pressure anisotropy value arises mainly from the balance between the collisionless creation term $2P(\partial u/\partial x)$ on the l.h.s. and the collisional damping term on the r.h.s. When the kinetic equation is solved using a split-step scheme, during the advection stage only collisionless terms are taken into account and thus a non-physical pressure anisotropy δP will appear over a time step δt, the order of magnitude of which, according to equation (11), can be as high as

$$\delta P \approx \frac{P v_{\text{th}} \delta t}{L_g}$$

if velocities of the order of the thermal velocity v_{th} are present, and L_g is the gradient scalelength of the problem. This spurious viscous pressure will in turn perturb the hydrodynamics; the relative error made in the velocity u can be estimated from the second hydrodynamics equation above to be of order:

$$\frac{\delta u}{u} \approx \frac{\delta P \delta t}{mnL_g u} \approx \left(\frac{v_{\text{th}}\delta t}{L_g}\right)^2.$$

After the advection stage, the collision stage will bring the distribution back to its original quasi-Maxwellian state, and accordingly the spurious pressure anisotropy introduced during the advection stage will disappear, leaving however a perturbation of the velocity field of order $(v_{\text{th}}\delta t/L_g)^2$. We can thus conclude that the condition for the kinetic calculation to remain valid in the case of strongly collisional systems is not the very restrictive condition $\delta t \ll \tau_i$ but instead

$$\delta t \ll \frac{L_g}{v_{\text{th}}}.$$

Since for numerical accuracy we choose a space step δx much smaller than the gradient scalelength L_g, this condition is then not more restrictive than a CFL-type condition $v_{\text{th}}\delta t < \delta x$.

A problem still remains on interfaces between strongly and weakly collisional regions, such as the hot-spot/dense-fuel interface in ICF targets, since in those regions there can be both a time step larger than the smallest value of the collision time and a short gradient length. However in those regions the meaningful length is not the local value of the thermal mean free path, but rather the slowing-down distance for particles from the hot zone through collisions with particles in the cold and dense zone. In a transition layer where the pressure balance relationship $nv_{\text{th}}^2 = \text{constant}$ holds, such as the hot-spot/dense-fuel interface in an ICF target [12], the local collision mean free path $\lambda_c \approx v_{\text{th}}^4/n$ goes like $1/n^3$ moving from one zone to the other, whereas the mean free path for hot particles colliding onto local thermal particles goes like $1/n$ only, so that the corresponding time step constraint is much less stringent.

In any case using too large a value for δt will only result in an exaggeration of the non-collisional features of the distribution, for example overestimating the ion heat flux and pressure anisotropy. But the excess values can be detected because they will tend to scale linearly with the time step. It is thus necessary to check by running several calculations with different time step values that the observed heat fluxes and temperature anisotropy do not strongly depend on the time step.

Conversely, in weakly collisional regions (for example in the central part of the target where shock-heated tenuous gas is standing) one should expect distributions made out of two parts, namely, a cold component consisting of the gas initially present in the target core, and a hot component arising from fast particle advection from zones previously heated by the main shock. This feature should not be mistaken for a numerical artefact, taking into account the collision time in that region, but care must be taken that it is not exaggerated by the numerical diffusion of the advection scheme, which in addition could lead to numerical problems if the cold component becomes too much localized and peaked.

3 Simulation and results for the implosion of a deuterium gas-filled target

We performed a kinetic simulation of the implosion of a 20 μm thick, 914 μm inner diameter CH shell filled with 15 atm of D_2 gas at room temperature, irradiated by a square laser pulse 1 ns in duration. The reference hydrodynamics simulation of that target was done with the code LILAC and is described in reference [9]. As explained in Section 2.3, the initial condition was calculated from the hydrodynamic profiles at time 500 ps, that is near the main shock outbreak into the fuel (see Fig. 1). The boundary condition on the fuel outer surface was deduced from the hydrodynamic state of the plasma in the last fuel cell of the LILAC simulation in the course of time. The numerical grid used 200 cells of equal thickness in space and 129×64 cells in velocity space $(v_r, v_\perp)$. A 1 ps time step was used. Differences between the hydrodynamic and

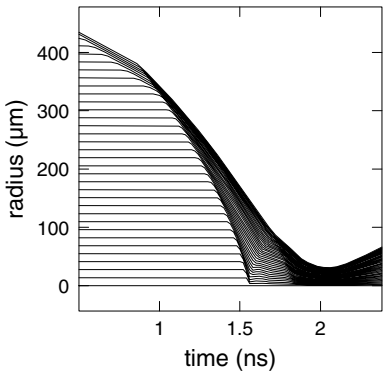

Fig. 1. Space-time diagram of the fuel in the hydrodynamic simulation of a D_2-filled CH shell, starting at the time of the main shock breakout into the fuel $t \approx 500$ ps.

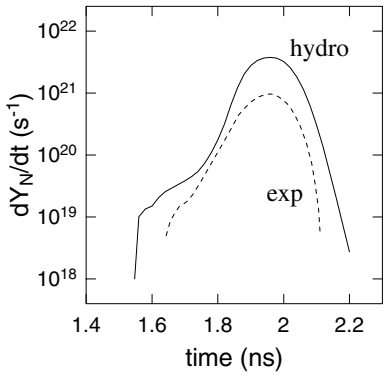

Fig. 2. The $D(D,n)^3He$ neutron production rate is plotted as a function of time, as measured in the experiment (exp) and as computed in the 1D LILAC hydrodynamics simulation (hydro). To cope with timing uncertainties in both the experimental results and the fluid simulation (due to the choice of the heat conduction flux limiter) the time origins of the curves were adjusted so that the absolute maximum of the yield occurs at the same time.

Fokker-Planck simulations are observed in three successive stages, as described in the following sections.

3.1 Shock propagation stage

During convergence of the main shock towards the centre of the target, a precursor can be observed in the Fokker-Planck simulation ahead of the imploding D_2. The shock structure is also broader and more complex than in the hydrodynamics simulation (see Fig. 3). In particular a large ion pressure anisotropy shows up inside the shock front. The shock width can be checked to be of the expected order of magnitude by estimating the slowing-down distance for ions from the central part of the target entering the shock front:

$$\lambda_{ii} = \frac{(m_D v_{\rm impl}^2)^2}{4\pi e^4 n_D \mathrm{Log}\Lambda_{ii}} \approx 20\ \mu\mathrm{m}$$

inserting figures corresponding to Figure 3, namely an implosion velocity $v_{\rm impl} \approx 5 \times 10^7$ cm/s and an ion density

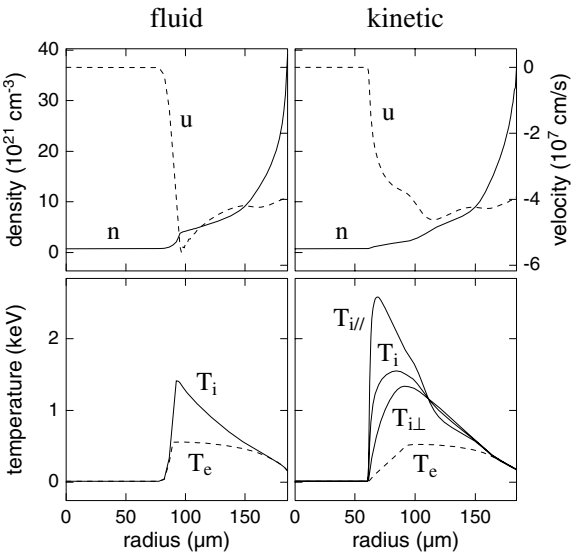

Fig. 3. Profiles of the density (n) and velocity (u) (top), of the electron (T_e) and parallel ($T_{i\|}$), perpendicular ($T_{i\perp}$) and total (T_i) ion temperatures (bottom) in the fuel at $t = 1460$ ps in a D_2 target implosion; left: fluid simulation results, right: kinetic simulation results.

$n_D \approx 4 \times 10^{21}$ cm^{-3} in the region downstream from the shock front. The detailed features of the shock structure are of course not correctly captured in the hydrodynamics simulation where the ion-shock width is artificially fixed to a few meshes by pseudoviscosity, and only the ion-electron temperature decoupling and relaxation can be rendered.

3.2 Shock convergence

When the main shock reaches the target centre, due to the shock precursor the Fokker-Planck simulation behaves quite differently from the fluid calculation (see Fig. 4): while the latter displays a sharp reflected shock front followed by a stagnating region where the density and temperature are high ($n = 5 \times 10^{22}$ cm^{-3} and $T_i = 13$ keV at $t = 1560$ ps), in the kinetic calculation the profiles are much smoother and compression goes on more gently in the centre: the ion temperature reaches a rather flat peak value around 6 keV while the density increases steadily from 1 to 6×10^{22} cm^{-3} between 1560 and 1700 ps. The ion temperature is lower in the centre of the target but higher in the outer part (for $r \gtrsim 20\ \mu$m).

3.3 Compression stage

At later times (see Figs. 5 and 6), the density and temperature profiles for either type of calculation come closer to each other, although at late times the temperature tends to remain higher in the kinetic simulation: the central hotter and denser region which can be seen in the fluid simulation shortly after the main shock convergence (see Fig. 4) has disappeared by $t = 1700$ ps (see Fig. 5).

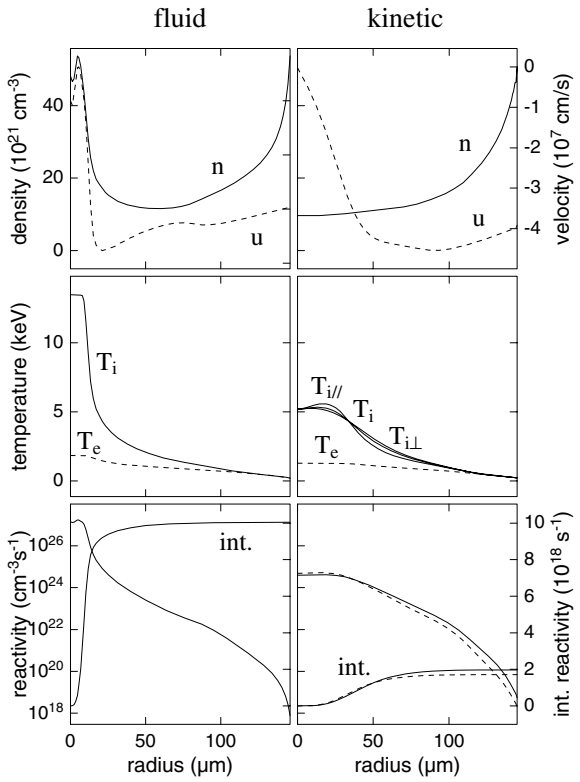

Fig. 4. Profiles of the density (n) and velocity (u) (top), of the electron (T_e) and parallel ($T_{i\|}$), perpendicular ($T_{i\perp}$) and total (T_i) ion temperatures (middle) and of the D(D, n)^{3}He reaction rate (bottom) in the fuel at $t = 1560$ ps in a D_2 target implosion; left: fluid simulation results, right: kinetic simulation results. In the kinetic case the reactivity is calculated using the exact distribution (solid lines) or the equivalent Maxwellian (dashed lines). Curves with the "int." label are plots of the reaction rate integrated over volume from the target centre.

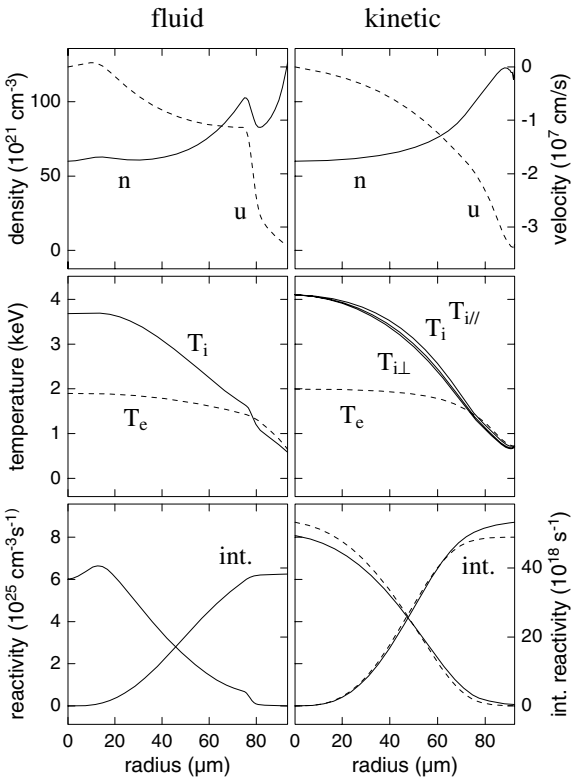

Fig. 5. Profiles of the density (n) and velocity (u) (top), of the electron (T_e) and parallel ($T_{i\|}$), perpendicular ($T_{i\perp}$) and total (T_i) ion temperatures (middle) and of the D(D, n)^{3}He reaction rate (bottom) in the fuel at $t = 1700$ ps in a D_2 target implosion; left: fluid simulation results, right: kinetic simulation results. In the kinetic case the reactivity is calculated using the exact distribution (solid lines) or the equivalent Maxwellian (dashed lines). Curves with the "int." label are plots of the reaction rate integrated over volume from the target centre.

This is particularly true in the case of the ion temperature: the electron-ion temperature decoupling is stronger in the kinetic simulation. At $t = 1900$ ps, which is shortly before maximal compression and just before the peak of the neutron yield, the hydrodynamic profiles are very close to each other, the main difference lying in a slightly higher ion temperature in the kinetic results, leading to a higher neutron yield (see Fig. 6). After stagnation, the expansion stage starts, in which the ion temperature is slightly lower in the Fokker-Planck simulation.

3.4 Neutron yield

The neutron production rate $\partial Y_N/\partial t$ for the reaction $D + D \rightarrow n + {}^3He$ calculated as described in Section 2.2.6 is shown in Figure 7 as a function of time for both simulations. The neutron yield decrease due to the kinetic behaviour of the ions predicted in references [4,5] is seen to occur only in the early part of the first neutron burst arising from the main shock convergence. Later on, the reaction rate of the kinetic simulation catches up with the fluid simulation rate and remains higher all over the compression stage (the stagnation of the pusher takes place around $t = 2050$ ps). During the subsequent expansion phase the calculated rates are essentially equal, with a slightly lower Fokker-Planck value due to the slightly lower ion temperature.

Figure 8 displays profiles of the reaction rate per unit radius $\partial^2 Y_N/\partial r \partial t$ at the same times as above for the fluid and kinetic calculations. These plots show which parts of the target contribute the most to neutron production, taking into account spherical geometry effects in addition to the variations of the local reactivity. We notice that although the reaction rate per unit volume is higher at or near the target centre (see the reactivity profiles in Figs. 4, 5 and 6), most of the yield comes from a shell which lies farther and farther away from the centre as time elapses. Due to this feature the neutron rate might be affected by Rayleigh-Taylor instabilities during the late part of the shock yield (see the profiles at $t = 1700$ ps in Fig. 8).

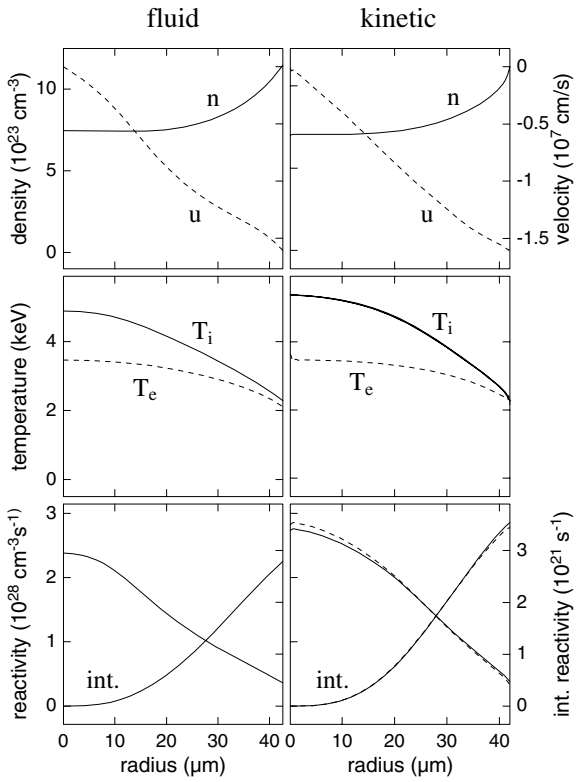

Fig. 6. Profiles of the density (n) and velocity (u) (top), of the electron (T_e) and ion (T_i) temperatures (middle) and of the $D(D,n)^3He$ reaction rate (bottom) in the fuel at $t = 1900$ ps in a D_2 target implosion; left: fluid simulation results, right: kinetic simulation results. In the kinetic case the reactivity is calculated using the exact distribution (solid lines) or the equivalent Maxwellian (dashed lines). Curves with the "int." label are plots of the reaction rate integrated over volume from the target centre.

4 Simulation and results for the implosion of an ICF ignition target

We started from a 1D spherical fluid simulation of the implosion of an ICF target with parameters typical of ignition capsules designed for the LMJ laser [11], namely 0.3 mg of cryogenic DT deposited on the inner surface of a CH shell of 1 mm (inner) radius. The space-time diagram of that simulation is displayed in Figure 9. Nuclear reactions were not taken into account to focus more specifically on the hydrodynamics of hot-spot formation during the implosion process. Nuclear reactivity will thus be calculated only as a post-processing diagnostics tool in the comparison of the fluid and kinetic simulations.

The kinetic calculation was started at $t = 17$ ns, when the main converging shock reaches the centre of the target. The boundary condition was taken from the hydrodynamic quantities recorded on the fuel/pusher interface (see Fig. 9) in the fluid simulation as a function of time. To treat in a satisfactory way both the dense region where the fluid simulation grid is the finest and the central zone where it is rather coarse, a spatial grid with a geometrically varying mesh size was used in the kinetic calculation,

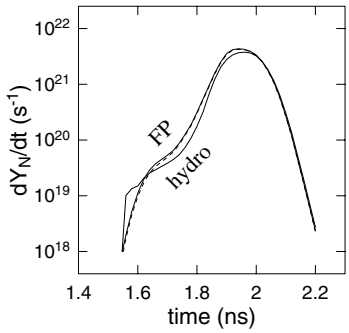

Fig. 7. Volume-integrated rate of the $D(D,n)^3He$ reaction as a function of time recorded in the kinetic (FP) and hydrodynamics (hydro) simulations. In the kinetic case the reactivity is calculated using the exact distribution (solid line) or the equivalent Maxwellian (dashed line).

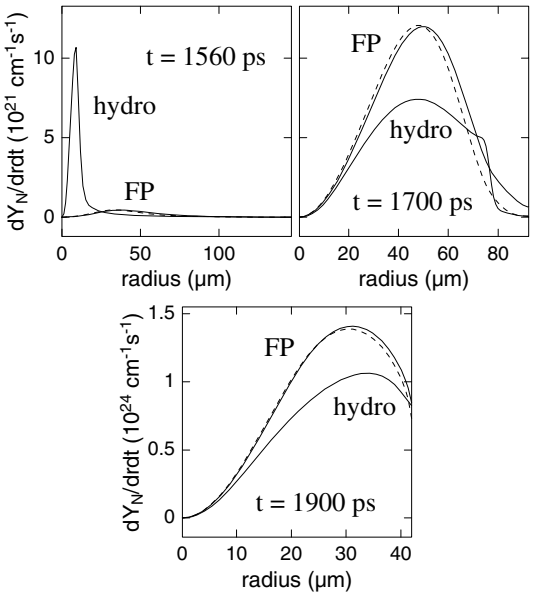

Fig. 8. Spatial profiles of the rate per unit radius of the $D(D,n)^3He$ reaction at three different times as recorded in the kinetic (FP) and hydrodynamics (hydro) simulations. In the kinetic case the reactivity is calculated using the exact distribution (solid lines) or the equivalent Maxwellian (dashed lines).

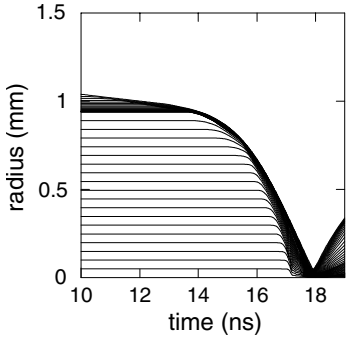

Fig. 9. Space-time diagram of the fuel in the hydrodynamic simulation of an LMJ ignition target with no nuclear reactions taken into account, starting at the time of the main shock breakout into the fuel $t \approx 10$ ns.

with a ratio of 0.95 starting from the pusher/fuel interface. Using the same number of cells (62) in the fuel as in the fluid calculation, the mesh size δr was thus decreasing from 20 μm near the centre to less than a micron near the outer boundary. The velocity space $(v_r, v_\perp)$ was discretized into 129×64 cells. Three runs were performed with time-step values of 0.25, 0.5 and 1 ps, to survey spurious non-collisional effects in very collisional regions as discussed in Section 2.3.2. Unless otherwise specified, all results shown in the following pertain to the smallest-time-step case.

To speed up the calculation, the D and T were not treated as separate species, but instead a single ion species with mass number 2.5 was used. This might affect the electron and ion temperature relaxation rate, since replacing a set of N ion species with densities n_i, mass numbers A_i and the same charge Z with a single species with a density equal to the total density $n = \sum n_i$ and a mass number equal to the mean value $A = \sum n_i A_i / \sum n_i$, neglecting the Coulomb logarithm variation, amounts to modifying the collisional relaxation term on the r.h.s. of equation (3) by a factor

$$\frac{\left(\sum_{i=1}^{N} n_i\right)^2}{\sum_{i=1}^{N} n_i A_i \sum_{i=1}^{N} \frac{n_i}{A_i}}.$$

In the present case of an equimolar DT mix, that factor is 0.96, or in other words a 4% reduction. This is a small, but non-negligible variation with respect to the differences in the electron-ion temperature decoupling recorded in the fluid and kinetic simulations. This effect can be corrected for in the FPion code by dividing the electron-ion collision rate in equation (3) by the same factor. Obviously that correction should also be applied to the electron collision term in the ion Fokker-Planck equation, to keep the total (electron + ion) energy conservation right, but this is automatically taken into account by the algorithm used in the code to treat electron-ion collisions.

However, using the above defined correction factor only leads to hardly noticeable temperature differences in the simulation. The discrepancies between the temperature profiles recorded in the fluid and kinetic calculations can thus not be explained by that effect.

As regards electron thermal conduction, the only effect of using a single ion species to model the DT mix, since D and T have the same Z, rests in a modification of the Coulomb logarithm (see definitions in Ref. [3]) which will be considered negligible.

The effect of the electric field on each ion species, taking the first two moments of the kinetic equation (1), can be written as:

$$A_i n_i \frac{\partial u_i}{\partial t} + A_i n_i u_i \frac{\partial u_i}{\partial r} = -\frac{n_i Z_i}{n_e} \frac{\partial P_e}{\partial r}.$$

Leaving aside species separation effects which obviously can only be treated using two different ion species, the velocity field u_i can be assumed not to depend on i ($u_i = u \; \forall i$), and hence summing the above equations over i leads to:

$$An \frac{\partial u}{\partial t} + Anu \frac{\partial u}{\partial r} = -\frac{\partial P_e}{\partial r}$$

where

$$n = \sum_i n_i \qquad \text{and} \qquad A = \frac{\sum_i n_i A_i}{\sum_i n_i}$$

so that the correct dynamics equation for a single species is recovered, taking into account the definition used for the mean mass number A, and thus no correction is needed.

Comparing the fluid and kinetic simulation results allows three successive stages to be identified, which will be described in more detail in the following sections. In the first, rather short, stage, non-collisional features (ion heat flux and ion pressure anisotropy) start developing without significant modifications of the plasma flow. Those features will progressively lead, in a second stage, to modifications in the main hydrodynamic quantities (density, velocity, temperature) as compared with the fluid simulation. The third stage is the vicinity of stagnation, which will be considered to lie between the time of the ion temperature peak in the centre of the target and the time of the maximum value of the overall fuel ρr.

4.1 First stage — Setup of non-collisional features

In this first stage, lasting approximately 100 ps after the beginning of the kinetic simulation (*i.e.* up to $t = 17.1$ ns after the beginning of the implosion), a high ion heat flux and a large ion pressure anisotropy build up in the less dense region of the system, with otherwise no noticeable modification of the density and velocity profiles. More specifically shock convergence in the centre occurs in much the same conditions as in the fluid simulation. This is displayed in Figure 10 for the main hydrodynamic quantities (density, velocity and parallel and perpendicular temperatures) and in Figure 11 for the heat flux. It can be noticed that the ion heat flux calculated by FPion is of the same order of magnitude as the electron heat flux in the central part of the target; such values cannot be reproduced by a classical model such as a flux-limited Spitzer conductivity. On one hand, the ratio of the heat flux to the free-streaming flux reaches very high values (see Fig. 11), and on the other hand those values are related to large values of the ion temperature anisotropy in the region considered (see Fig. 10).

The high ion heat flux tends to smooth out the peak of the ion temperature T_i observed in the target centre, and in addition the electron temperature is slightly lower than in the fluid simulation, which cannot be explained by the modeling of the collisional processes at work (see the above discussion).

The quick transition which takes place during this first stage of the kinetic simulation to a regime with markedly non-collisional features possibly indicates that the kinetic calculation should be started earlier in the implosion process, since those effects might have non-negligible consequences during the initial DT acceleration phase, before

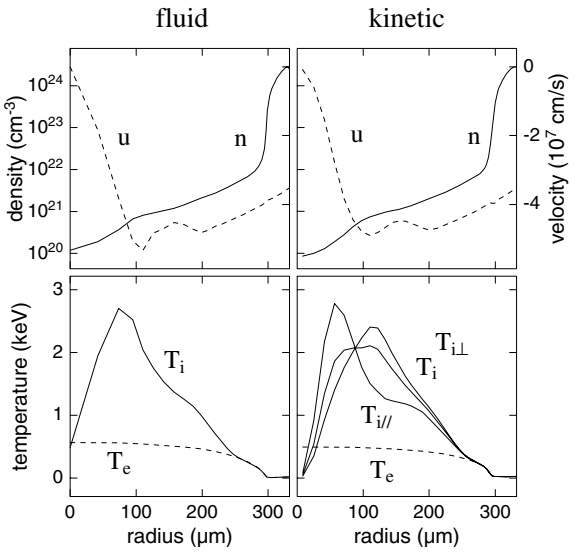

Fig. 10. Profiles of the density (n) and velocity (u) (top), of the electron (T_e) and parallel ($T_{i\|}$), perpendicular ($T_{i\perp}$) and total (T_i) ion temperatures (bottom) in the fuel at $t = 17.1$ ns in a DT ignition target implosion; left: fluid simulation results, right: kinetic simulation results.

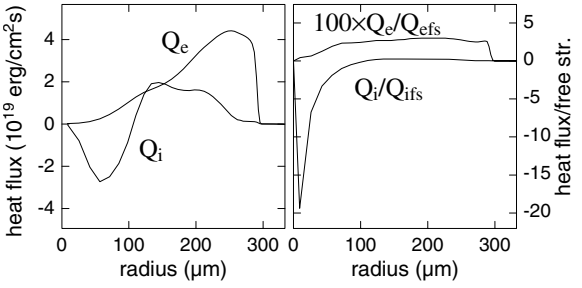

Fig. 11. Profiles of the ion (Q_i) and electron (Q_e) heat fluxes (left) and of the ratio of the heat flux to the free-streaming heat flux (right) for ions (Q_i/Q_{ifs}) and electrons (Q_e/Q_{efs}) in the fuel at $t = 17.1$ ns in the kinetic simulation of a DT ignition target implosion. The time step used in this case was $\delta t = 0.25$ ps. The flux/free-streaming flux ratio for electrons is displayed with a hundredfold magnification factor.

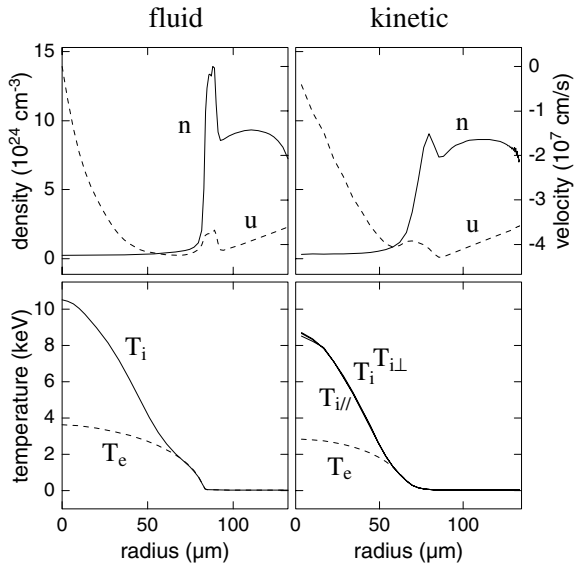

Fig. 12. Profiles of the density (n) and velocity (u) (top), of the electron (T_e) and parallel ($T_{i\|}$), perpendicular ($T_{i\perp}$) and total (T_i) ion temperatures (bottom) in the fuel at $t = 17.65$ ns in a DT ignition target implosion; left: fluid simulation results, right: kinetic simulation results.

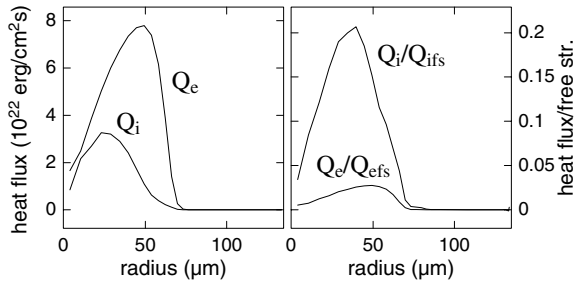

Fig. 13. Profiles of the ion (Q_i) and electron (Q_e) heat fluxes (left) and of the ratio of the heat flux to the free-streaming heat flux (right) for ions (Q_i/Q_{ifs}) and electrons (Q_e/Q_{efs}) in the fuel at $t = 17.65$ ns in the kinetic simulation of a DT ignition target implosion. The time step used in this case was $\delta t = 0.25$ ps.

the main shock convergence. This would make the computation much more costly in terms of computing time, and has thus not been attempted so far, since treating the shock break-out from the dense DT layer implies starting the computation before $t = 14$ ns (see Fig. 9), which, at the very least, amounts to a four-fold increase in computing time, not even taking into account the greatly increased collisionality in the dense and cold DT at that time.

4.2 Second stage — Non-collisional effects on implosion

In this second stage which extends up to the vicinity of stagnation, the features which emerged in the previous stage become progressively stronger and their effects on the flow accumulate. This is evidenced by the profiles of hydrodynamic quantities at time $t = 17.65$ ns (which is the time of maximum ion temperature in the centre of the target in the kinetic simulation). Figure 12 displays the main hydrodynamic quantities (density, velocity, parallel and perpendicular temperatures) in both simulations, and Figure 13 the heat fluxes at the same time, taken from the kinetic simulation with the smallest time step $\delta t = 0.25$ ps. The electron and ion temperatures are noticeably lower in the kinetic case due to the large outbound ion heat flux. The ion temperature is now almost isotropic (see Fig. 12), and the ion heat flux has come down to more reasonable values with respect to the electron heat flux, although the heat-flux/free-streaming-flux ratio is still much larger for the ions than for the electrons (see Fig. 13). The compression zone which will ultimately become the dense fuel shell at stagnation (the negative velocity gradient region

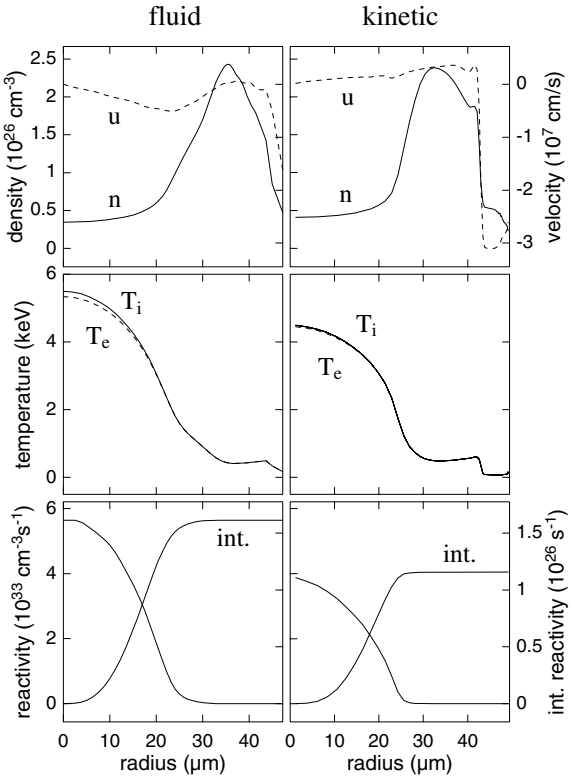

Fig. 14. Profiles of the density (n) and velocity (u) (top), of the electron (T_e) and ion (T_i) temperatures (middle) and of the D(T, n)^{4}He reaction rate (bottom) in the fuel at $t = 17.9$ ns in a DT ignition target implosion; left: fluid simulation results, right: kinetic simulation results. The reactivity is calculated using the equivalent Maxwellian. Curves with the "int." label are plots of the reaction rate integrated over volume from the target centre.

about $r = 60{-}80$ μm in Fig. 12) now lies closer to the target centre.

4.3 Third stage — Vicinity of stagnation

In the fluid simulation at $t = 17.9$ ns, the density reaches its maximum, the densest part of the fuel is stagnating (velocity $u \approx 0$) while expanding on both sides, and 30 ps later the reflected shock has swept over the whole fuel, reversing the velocity of the pusher/fuel interface. At the same time the DT ρr goes through a smooth maximum of about 2.2 g/cm^2. Figure 14 displays profiles of the hydrodynamic quantities in the fluid and kinetic simulations at $t = 17.9$ ns. Figure 15 shows the DT ρr profiles in both simulations at the same time.

Although the density profile is different in the kinetic simulation, the DT ρr profile is very similar, both in terms of its maximum value (which is the full fuel ρr) and of the hot-spot ρr. On the opposite, the maximum ion temperature reached in the hot spot is noticeably lower than in the fluid calculation, while the density there is higher, yielding an almost equal pressure. This points to an increased rate of ablation of the cold fuel by the large ion heat flux from

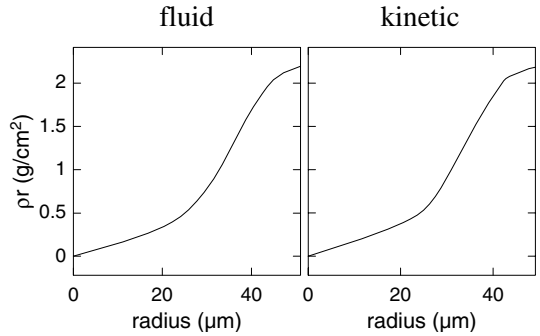

Fig. 15. Profile of the fuel ρr integrated from the centre at $t = 17.9$ ns in a DT ignition target implosion; left: fluid simulation results, right: kinetic simulation results.

the hot spot, although from the hot-spot temperature decrease alone the opposite should have been expected.

Let us finally discuss the effect of the modifications of the hydrodynamics on target performance. The rate of the thermonuclear reaction D + T $\rightarrow n + \alpha$ calculated as described in Section 2.2.6 at the end of the kinetic simulation is shown in Figure 14. In this case only values for the equivalent Maxwellian distribution were computed since independent distribution functions for D and T were not available. It can be noticed that, due to the lower ion temperature in the hot spot, both the local reaction rate (number of reactions per unit volume per second) and the volume-integrated rate (number of reactions per second) over the whole fuel are lower in the kinetic simulation. This should reduce the safety margin of the ignition process, although from the fuel ρr alone the final yield might not be reduced, at least from a rough estimate using formula (9) of reference [12] giving the final reaction fraction Φ as a function of DT ρr in g/cm^2:

$$\Phi \approx \frac{\rho r}{\rho r + 6}.$$

In summary the overall consequences of kinetic effects on burn seem contradictory. On one hand, the ignition threshold is expected to be raised since a lower reaction rate is obtained in the hot spot, but on the other hand the unmodified target ρr should preserve the overall burn fraction. This might point to the need of re-designing the target dimensions or the temporal power profile of the laser pulse used to drive the implosion, to increase the hot-spot efficiency while trying to keep the highest possible fuel ρr.

4.4 Effect of the time step on non-collisional features

As discussed in Section 2.3.2, it is necessary to check that the non-collisional features (ion heat flux and pressure anisotropy) emerging in the kinetic simulation are not just artefacts due to the time step being much greater than the collision time (at least in the colder and denser parts of the target). It is not possible in practice to run a reference case with a time step of the same order of the smallest collision

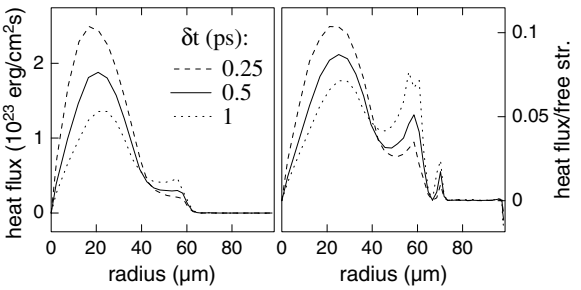

Fig. 16. Profiles of the ion heat flux (left) and heat flux/free-streaming flux ratio (right) at $t = 17.75$ ns in the kinetic simulation of a DT ignition target implosion for three different values of the time step $\delta t = 0.25$, 0.5 and 1 ps.

time encountered in the system, but at least it is necessary to check that the non-collisional features observed do not depend linearly on the time step, which would identify them as entirely numerical. For that purpose, three cases were run with different time step values $\delta t = 0.25$, 0.5 and 1 ps, and otherwise identical. The ion heat flux profiles obtained at time $t = 17.75$ ns in the three cases are displayed in Figure 16. The maximum variation of the heat flux and its ratio to the free-streaming flux do not exceed a factor 2 (in the denser region) while the time step is varied by a factor 4. It can be thus assumed that the order of magnitude of the observed fluxes is right, even though the value obtained in the denser part of the fuel is not accurate. Let us also notice that in the mildly collisional region where the absolute maximum of the heat flux is recorded, the latter scales in the opposite way with the time step, but this is now a physical effect due to different temperature profiles.

5 Summary and discussion

Significant improvements were made to the ion Fokker-Planck code FPion, which now allow the simulation of systems of macroscopic size, beyond the more academic cases studied in the past, such as the structure of plasma shock-wave fronts [6]. That new version of the code was applied to the laser implosion of D_2-gas-filled capsules as well as the problem of the hot-spot formation in ICF targets such as those which will be used with next-generation megajoule-size lasers. Detailed comparisons with existing hydrodynamics simulations of the same targets were performed, using various diagnostics including post-processed nuclear reactivities (in the work done so far nuclear reactions were not taken into account "in line" in the simulations).

The main consequence of properly taking into account the weaker collisionality of the plasma in the central part of those targets through a fully kinetic calculation is an increased thermal energy transfer between the target core and its surroundings during the implosion, leading to a modified ion temperature.

In the case of D_2-gas targets, this leads to a decrease of the maximum ion temperature at the time of the main shock collapse in the centre, and conversely a higher temperature during the ensuing compression stage. As a consequence, the shock-related neutron yield is lowered, which brings the simulation results in better agreement with experiments as regards that part of the neutron curve, but the compression yield is slightly increased, which makes the comparison with experiment even worse there. From the observed location of the main part of the yield inside the target, if the explanation of that discrepancy by hydrodynamic instabilities is to be retained, then this implies that the corresponding fuel/pusher mix should affect most of the target volume.

In the case of ignition DT targets, those effects lead to a stronger cooling of the target core, with a comparable pressure in the fuel due to the increased rate of ablation of the dense layer by the heat flux from the hot spot. Although the details of the density profile at stagnation are different, no significant change of the hot-spot or overall target ρr is found. Consequences on ignition are, on one hand, a decreased ignition safety from the lower reaction rate in the hot spot, but on the other hand no expected reduction in the final yield of the target. However a more definite conclusion on the latter point has to wait until a full kinetic simulation of ignition including an in-line treatment of nuclear combustion and hot reaction products becomes feasible. An additional effect which could be investigated with the present version of the code is the possible D/T species separation which might modify the hot-spot reactivity.

Some improvements may however be already considered at this point. Among other things, it might be necessary to start the kinetic simulation earlier before the main shock convergence since kinetic features build up very soon after the beginning of the Fokker-Planck calculation (see Sect. 4.1) and lead to significant modifications of the hydrodynamics in the mildly collisional region of the target, and such effects might occur much earlier in the course of the implosion process.

A comparison of the evolution of the spatial discretization grid during implosion in the fluid and kinetic simulations suggests that the FPion code should be improved in that respect, for example by implementing some kind of "quasi-Lagrangian" scheme such as the one used in our multifluid hydrodynamics code MULTIF [20]. The zoning scheme used here is well adapted to the earlier part of the simulation, but not so much near stagnation since the density peak at that time does not involve the same fuel layers as in the beginning. Besides, it can be checked that the total DT mass is not strictly conserved in the kinetic calculation, due to the specific boundary condition used which imposes no constraint on outgoing particles. A more accurate comparison with fluid results might thus need a mirror-type boundary condition.

From the point of view of the underlying physical model, it might seem necessary to take into account dense-plasma effects (beyond electron degeneracy which is included in the code in its present state) since the values of the Coulomb logarithms found are small in the dense and cold main fuel layer. The Fokker-Planck collision term

included in FPion is not supposed to remain valid in such conditions. However in the present case this problem should be mitigated by the fact that the pusher motion is taken as is from the fluid simulation with no modification from the different behaviour of the fuel. This latter feature of our simulations might be changed in favor of some kind of hybrid model which would perform a fluid treatment of most of the system while self-consistently including a kinetic treatment of the fuel, or dynamically shift to a kinetic model in mildly collisional regions in the spirit of reference [36].

Finally the main part of the work which remains to be done as regards the investigation of ion-kinetic effects in ICF target ignition involves the self-consistent treatment of nuclear reactions and combustion, beyond the simple energy-deposition models implemented in present-day fluid codes [37]. This demands that ion species with a much higher temperature be treated together with the colder imploding plasma in the kinetic code, which implies an important physical and numerical development effort.

We acknowledge fruitful discussions with J.A. Delettrez and Y. Saillard, who also kindly provided us with results from their numerical simulations, on which this work is based.

References

1. S. Atzeni, Plasma Phys. Contr. Fusion **29**, 1535 (1987)
2. L. Spitzer, R. Härm, Phys. Rev. **89**, 977 (1953)
3. S.I. Braginskii, *Transport Processes in a Plasma*, Reviews of Plasma Physics, edited by M.A. Leontovich (Consultants Bureau, New York, 1965), p. 205, Vol. 1
4. A.G. Petschek, D.B. Henderson, Nucl. Fusion **19**, 1678 (1979)
5. T. Nishikawa, H. Takabe, K. Mima, Jpn J. Appl. Phys. **28**, 2004 (1989)
6. M. Casanova, O. Larroche, J.-P. Matte, Phys. Rev. Lett. **67**, 2143 (1991)
7. F. Vidal, J.-P. Matte, M. Casanova, O. Larroche, Phys. Rev. E **52**, 4568 (1995)
8. T. Yabe, K.A. Tanaka, Laser Part. Beams **7**, 259 (1989)
9. J.A. Delettrez *et al.*, *31st Annual Anomalous Absorption Conference* (Sedona, AZ, USA, 3-8 June 2001), Paper O5-1
10. P.A. Bradley, D.C. Wilson, Phys. Plasmas **8**, 3724 (2001) and references therein
11. Y. Saillard, C. R. Acad. Sci. Paris t. 1 **IV**, 705 (2000)
12. J.D. Lindl, Phys. Plasmas **2**, 3933 (1995)
13. E.G. Gamaly, *Hydrodynamic Instability of Target Implosion in ICF*, in *Nuclear Fusion by Inertial Confinement – A Comprehensive Treatise*, edited by G. Velarde, Y. Ronen, J.M. Martínez-Val (CRC Press, Boca Raton, Florida, 1993), Chap. 13, p. 321
14. N. Hoffmann, *Hydrodynamic Instabilities in Inertial Confinement Fusion*, in *Laser Plasma Interactions 5: Inertial Confinement Fusion*, edited by M.B. Hooper (SUSSP Publications, Edinburgh and IOP Publishing, London, 1995), p. 105
15. S.E. Bodner *et al.*, Phys. Plasmas **5**, 1901 (1998)
16. C. Bayer *et al.*, Nucl. Fusion **24**, 573 (1984)
17. M.N. Rosenbluth, W.M. MacDonald, D.L. Judd, Phys. Rev. **107**, 1 (1957)
18. T.A. Mehlhorn, J.J. Duderstadt, J. Comput. Phys. **38**, 86 (1980)
19. J.J. Honrubia, *Charged-Particle Transport in ICF Targets*, in *Nuclear Fusion by Inertial Confinement – A Comprehensive Treatise*, edited by G. Velarde, Y. Ronen, J.M. Martínez-Val (CRC Press, Boca Raton, Florida, 1993), Chap. 9, p. 211
20. C. Chenais-Popovics *et al.*, Phys. Plasmas **4**, 190 (1997)
21. K. Huang, *Statistical Mechanics* (John Wiley & Sons, New York, 1965)
22. D.L. Book, *NRL Plasma Formulary*, NRL Publication 177-4405 (Naval Research Laboratory, Washington, 1990)
23. O. Larroche, Phys. Fluids B **5**, 2816 (1993)
24. J.J. Honrubia, J.M. Aragonés, Nucl. Sci. Eng. **93**, 386 (1986)
25. T.M. Tran, J. Ligou, Nucl. Sci. Eng. **79**, 269 (1981)
26. C.Z. Cheng, G. Knorr, J. Comput. Phys. **22**, 330 (1976)
27. L. Demeio, J. Comput. Phys. **99**, 203 (1992)
28. E. Sonnendrücker, J. Roche, P. Bertrand, A. Ghizzo, J. Comput. Phys. **149**, 201 (1999)
29. A.J. Klimas, W.M. Farrell, J. Comput. Phys. **110**, 150 (1994)
30. C. de Boor, *A Practical Guide to Splines* (Springer-Verlag, New York, 1978)
31. G.I. Marchuk, *Methods of Numerical Mathematics* (Springer-Verlag, New York, 1982)
32. P.M. Morse, H. Feshbach, *Methods of Theoretical Physics* (McGraw-Hill, 1953)
33. P.L. Bhatnagar, E.P. Gross, M. Krook, Phys. Rev. **94**, 511 (1954)
34. J.M. Greene, Phys. Fluids **16**, 2022 (1973)
35. H.-S. Bosch, G.M. Hale, Nucl. Fusion **32**, 611 (1992)
36. P.W. Rambo, J. Denavit, *Multi-Fluid Modeling of Interpenetrating Plasmas*, Proceedings of the CECAM Workshop on Ion-Kinetic Effects in Laser-Produced Plasmas (Orsay, France, 1992), p. 75
37. E.G. Corman, W.E. Loewe, G.E. Cooper, A.M. Winslow, Nucl. Fusion **15**, 377 (1975)